Journal of Inorganic and Organometallic Polymers and Materials
https://doi.org/10.1007/s10904-020-01634-2

Polymer Precursors Effect in the Macromolecular Metal-Polymer on the $Rh/RhO_2/Rh_2O_3$ Phase Using Solvent-Less Synthesis and Its Photocatalytic Activity

C. Diaz[1] · M. L. Valenzuela[2] · O. Cifuentes-Vaca[3] · M. Segovia[1]

Received: 1 April 2020 / Accepted: 18 June 2020

Abstract
A mixture of a nanostructured Rh/RhO_2 phase was easily obtained by thermally treating the macromolecular Chitosan·$(RhCl_3)_x$ precursor, while the Rh/Rh_2O_3 phase was obtained by pyrolyzing PSP-4-PVP·$(RhCl_3)_x$ precursors. The nature of the polymeric precursor acting as a solid-state template does not significantly influence the "foam-like" morphology of the Rh/RhO_2 and Rh/Rh_2O_3 nanoparticles. The size of the obtained products is within the range of 16 nm, as confirmed by HRTEM. A possible formation of the Rh/RhO_2 and Rh/Rh_2O_3 nanoparticles is proposed. The bandgap values estimated from Tauc plots are 3.7 eV, and 3.0 eV for Rh/RhO_2 and Rh_2O_3, respectively. Their photocatalytic activity was measured, for the first time, using a methylene blue pollutant, achieving a photodegradation of 78% for Rh/RhO_2 and 70% for Rh/Rh_2O_3 in 300 min.

1 Introduction

From the precious metals of the periodic table, the Ir, Rh Pd, and Pt are the most catalytically active [1], and their activity is hugely enhanced at the nano-level [2, 3]. Among these, rhodium plays an essential role in several catalytic applications [4, 5]. However, the catalytic mechanism of rhodium materials is still elusive. Recent investigations suggest that the active centers could be in rhodium oxide rather than rhodium [5, 6], and the most common rhodium oxides are Rh_2O_3 and RhO_2. Although they have a wide range of applications in catalysis, scarce preparation methods of nanostructured Rh_2O_3 and RhO_2 have been reported, and their morphological and size control remains poorly known [4, 5, 7–9]. All the described Rh_2O_3 preparation methods are solution-based and solid-state methods that have not been reported yet. For instance, $Rh(NO_3)_3$ [7, 8], usually produces Rh oxides leading to RhO_2 and RhO_2 mixtures. Different mixtures can be obtained based on the thermal treatment temperature [8]. A mixture of α-and β-Rh_2O_3 can be obtained by heating to 797 °C, while a further increase up to 1000 °C is required to obtain pure β-Rh_2O_3 [8]. Besides, Rh_2O_3 nanosheet assemblies have been prepared by oxidizing ultrathin Rh nanosheet with $HClO_4$ [5]. Finally, Rh oxide nanofibers have been also prepared using electrospinning procedures [4].

In this study, we report the first general solid-state method to prepare Rh/Rh_2O_3 and Rh/RhO_2 nanostructured materials [10–12]. Regarding the possible application of these Rh metal oxides, the first step is usually their incorporation into solid matrices. Additionally, considering that these nanoparticles will be used in real solid devices involving high-temperature procedures, the metal oxides inside the matrix must be stable [13, 14]. In this sense, the incorporation of metal-oxide nanoparticles into solid devices is not straightforward when they are produced via a solution-phase method [13, 14], since the solid-state isolation of nanoparticles usually causes agglomeration [15–18]. Thereupon, the incorporation of metal-oxide nanoparticles generated directly from a

Electronic supplementary material The online version of this article (https://doi.org/10.1007/s10904-020-01634-2) contains supplementary material, which is available to authorized users.

✉ C. Diaz
c.diaz@uchile.cl

✉ M. L. Valenzuela
maria.valenzuela@uautonoma.cl

[1] Departamento de Química, Facultad de Química, Universidad de Chile, La Palmeras 3425, Nuñoa, Casilla 653, Santiago de Chile, Chile

[2] Instituto de Ciencias Químicas Aplicadas, Facultad de Ingeniería, Universidad Autónoma de Chile, Llano Subercaseaux 2801, San Miguel, Santiago de Chile, Chile

[3] Facultad de Ciencias Exactas, Universidad Andrés Bello, Concepción, Autopista Concepción-Talcahuano 7100, Talcahuano, Chile

Published online: 04 July 2020

solid-state approach appears to be the most reliable method. Thus, both nanostructured materials (Rh/Rh_2O_3 and Rh/RhO_2) obtained by the described solid-state method, could be potentially a better catalyst than the isolated Rh or the Rh_2O_3 and RhO_2 oxides [5, 6].

A representation of the general method to prepare nanostructured Rh/RhO_2 and Rh/Rh_2O_3 is shown in Scheme 1.

2 Material and Methods

2.1 Preparation of Polymer–Metal Complexes

In 20 ml dichloromethane, a stoichiometric polymer amount (1:1 polymer:complex) and 0.40 g of metal complexes were added. The heterogeneous mixture was stirred at room temperature (RT) for 8th days. The obtained solid was washed with dichloromethane and dried under vacuum for 3 h. Pyrolysis: The polymer-metal complexes were pyrolyzed in a box furnace (lab tech) at 800 ºC. Additional details of the experimental procedures are given in Table 1 of Supporting Information S1.

2.2 Characterization

IR spectra were recorded using an FT-IR Perkin-Elmer 2000 Spectrophotometer. Scanning electron microscopy (SEM) was performed on a JEOL 5410 scanning electron microscope. Elemental microanalysis was performed by energy dispersive X-ray analysis (EDS) using a NORAN Instrument micro-probe attached to the SEM. High-Resolution Transmission Electron Microscopy (HR-TEM) was performed using a JEOL 2000FX TEM microscope at 200 kV to determine the average particle size, distribution, elemental composition, and crystallinity of samples. The average particle size was calculated using Digital Micrograph software. 30 ml of a 1×10^{-5} M methylene blue (MB) solution was used to assess the photocatalytic activity of composites. The same mass amount (5.6 mg) was analyzed for each sample. Irradiation was performed with a 300 W xenon lamp model 6258 (incident light intensity of 1250 mW/m^2) and was measured with a pyrometer. The distance between the lamp and the suspension was 16 cm. The MB concentration for each sample was determined by UV–Vis spectrophotometry. Specifically, the maximum absorbance intensity corresponding to the lowest energy peak of the methylene blue characteristic spectrum at 664 nm was measured. The photocatalytic efficiency of the products was expressed as the degradation percentage variation regarding the irradiation time. The thermal gravimetric analysis was performed on a Perkin Elmer TGA 4000 instrument. Samples were heated at a rate of 10 °C/min from room temperature to 800 °C under constant nitrogen or air flow (20 ml/min).

3 Results and Discussion

The presence and coordination degree of $RhCl_3$ to the polymer backbone was performed by thermogravimetry analysis (TG) under air (see Supplementary Information S2). The pyrolytic residue corresponded to Rh/RhO_2 from the Chitosan·$(RhCl_3)_x$ precursor (chitosan from now on), while the one for the PSP-4-PVP·$(RhCl_3)_x$ precursor (PVP from now on) yielded Rh/Rh_2O_3. The coordination degree was estimated by mass difference compared with the macromolecular complexes with 100% coordination. Values

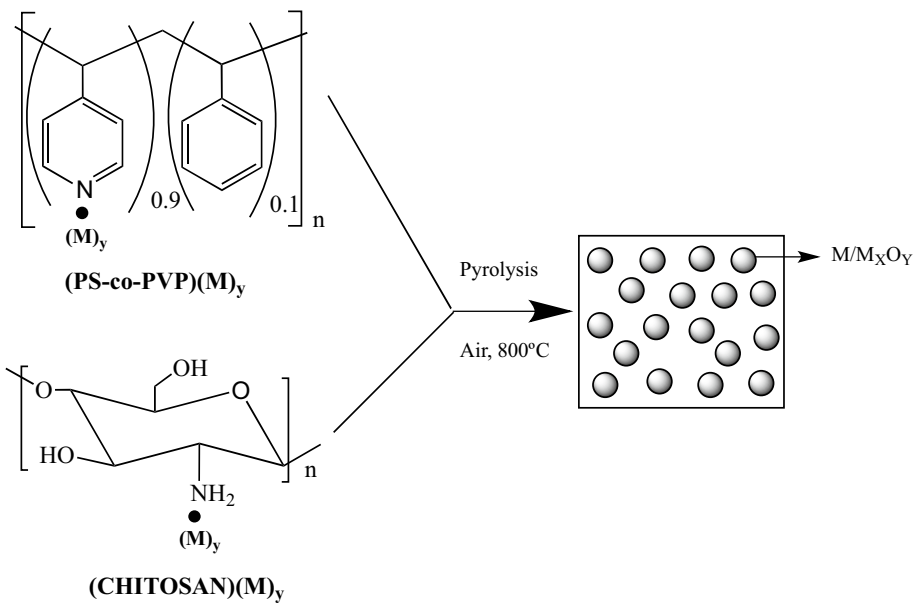

Scheme 1 General representation of the Rh/RhO_2 and Rh_2O_3 preparation

were 82.2% and 80.8% for the chitosan and PVP precursors, respectively. As a consequence, TG analysis confirmed the presence of both precursors slightly modified by the $RhCl_3$ coordination. For the chitosan precursor, the weight loss at 213 °C was assigned to the NH_2, CH_2OH, and OH groups decomposition (carbonization) to the main carbon ring of the chitosan. On the other hand, the weight loss at 540 °C was assigned to the decomposition of the chitosan carbon skeleton. Both weight losses were modified to temperatures lower than the free chitosan due to the polymer's coordination, which decreased the thermal stability as it is usually observed in these kinds of compounds. Exothermal processes accompanied these two main weight losses (see exothermal peaks at 213 °C and 540 °C). Conversely, the two main peaks at 340 °C and 456 °C for the PVP precursor (see Supplementary Material S2, B) were assigned to the weight loss of the pyridine and styrene groups decomposition, respectively. Again, these peaks appeared at temperatures lower than the free precursor without the coordination metal, at 388 °C, and 513 °C, respectively.

XRD patterns of the pyrolytic product from the chitosan precursor indicated a mixture of Rh/RhO_2 phases, as observed in Fig. 1a). Usually, Rh oxides mixtures are obtained, as Saric et al. reported different RhO_2/Rh_2O_3 mixtures based on the annealing temperature [7, 8]. Kibis et al. also studied Rh/RhO_x mixtures [9]. Furthermore, we obtained Rh/Rh_2O_3 phases (orthorhombic) using the PVP precursor (see Fig. 1b), and the Rh_2O_3 XRD pattern was consistent with JCPDF 00-043-0009.

SEM experiments were performed to characterize the morphology and size of particles. For the Rh/Rh_2O_3-PVP sample, a porous structured morphology was observed, with agglomerated particles ranging from 250 to 500 nm, as shown in Fig. 2a, b. Finally, a similar behavior was observed for the Rh/RhO_2-Chitosan sample, although in this case, the agglomerated particles seemed smaller (100–300 nm), as shown in Fig. 2c, d. These morphologies were not observed for Rh_2O_3, which was obtained from different solution preparation methods [4, 5, 7–9].

HR-TEM analysis was also performed, as shown in Fig. 3. An image of the Rh/Rh_2O_3 sample from the PVP precursor is shown in Fig. 3a. Typical particle sizes are ranging from 5 to 40 nm with a mean size of 16 nm according to histogram showed in Supplementary Material S3. Crystallinity was also confirmed by the interplanar distance observed in Fig. 3b (0.352 nm assigned to the 200 plane). As for the chitosan precursor, Rh/RhO_2 particles can be observed in Fig. 3c, with particle sizes ranging from 10 to 20 nm. However, it was not possible to acquire HR images for the Rh/Rh_2O_3 sample using the PVP precursor, as most of the particles formed agglomerates. In any case, EDS analysis confirmed the presence of both rhodium and oxygen, which is consistent with XRD's Rh/RhO2 mixtures.

3.1 Photocatalytic Activity of Rh/RhO_2 and Rh_2O_3 Materials Towards the Blue Methylene Pollutant

The main applied field of metallic Rh and rhodium oxides (RhO_2 and Rh_2O_3) is for developing electrocatalysis applications, including CO oxidation, H_2O_2 oxidation, and N_2O decomposition [5]. However, the photodegradation of pollutants using these Rh oxides have not been reported yet. Only a few works reported the Rh_2O_3 bandgap [19–22]. According to these studies, they agree that this value—estimated by the Tauc method—is within the range of 3.0 eV for Rh/Rh_2O_3. However, no estimation was reported for Rh/RhO_2. In this research, we calculated a value of 3.7 eV for our mixed Rh/RhO_2 phase, as described in Supplementary Material S4. This value suggests a photocatalytic activity in the visible region toward dyes pollutants [23]. The deactivation

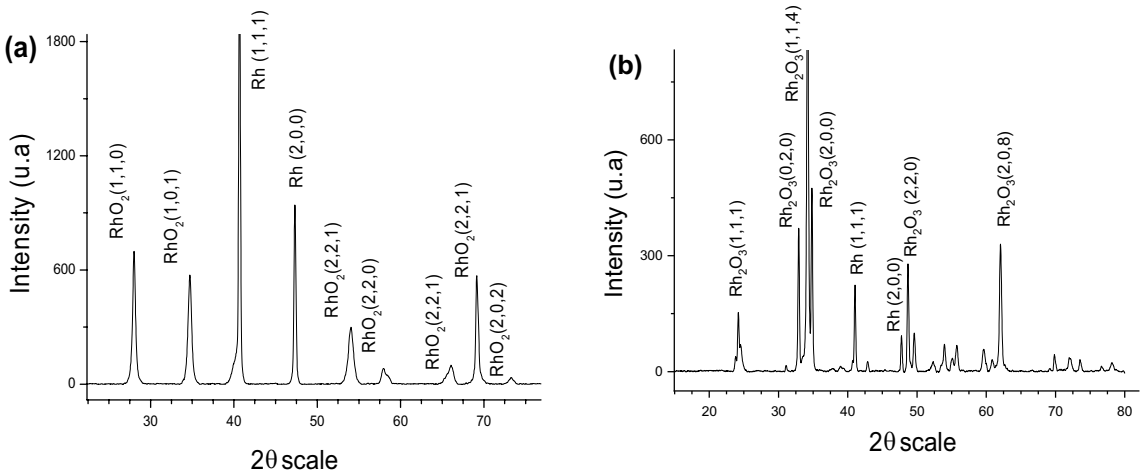

Fig. 1 Rh/RhO_2 XRD pattern obtained from precursors: **a** Chitosan·$(RhCl_3)_x$, and **b** Rh/Rh_2O_3 from PSP-4-PVP·$(RhCl_3)_x$

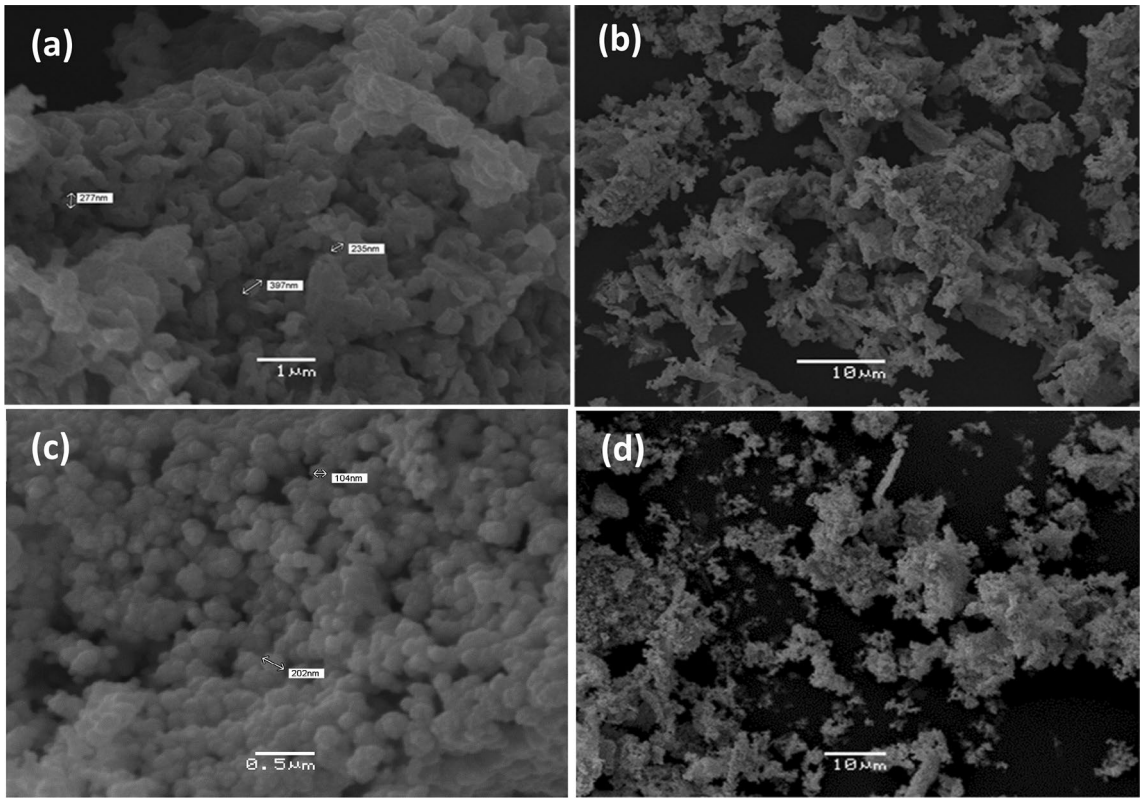

Fig. 2 SEM image for the Rh/Rh_2O_3-PVP sample (**a**), (**b**); Rh/RhO_2-Chitosan sample (**c**) and (**d**)

of methylene blue (MB) dye using both Rh/RhO_2 and Rh/Rh_2O_3 phases was studied under visible irradiation. Figure 4a shows the typical MB degradation rates with the pyrolytic products from both Chitosan and PVP precursors. The Rh/RhO_2 sample exhibited a better photocatalytic activity (78% photodegradation in 300 min) than the Rh/Rh_2O_3 (70% photodegradation in 300 min). The photocatalytic reaction of both compounds followed a first zero-order kinetic, as shown in Fig. S5a and b in Supporting Information. Finally, Supporting Information S6 shows the absorption spectrum of the MB solution at different degradation times for both Rh/RhO_2 and Rh/Rh_2O_3 compounds.

The photocatalytic activity of Rh/RhO_2 and Rh/Rh_2O_3 nanoparticles toward the methylene blue degradation are lesser than TiO_2 and Fe_2O_3 nanostructured materials, higher than ReO_3, IrO_2, and ThO_2, and just like NiO, as shown in Table 1. These results can be related to their bandgap values. Incidentally, an appropriate photocatalyst should work in the visible light region ($420\ nm < \lambda < 800\ nm$) with a bandgap near 3 eV. This outcome can explain the relatively-low photocatalytic activity for ThO_2, for instance.

3.2 Probable Formation Mechanism

Some insight about the formation mechanism of the nanostructured Rh metal oxides (from both precursors) can be proposed using the formation mechanism of nanostructured metallic materials from the oligomer precursor $NP(OC_8H_{12})_2(OC_6H_4PPh_2\text{-}Mn(CO)_2(\eta^5\text{-}C_5H_4Me)_2\}_n$ [24]. A schematic representation of this process is provided in Fig. 5. Briefly, the first step (heating) would be the formation of a 3D network to produce a thermally stable matrix. This step is crucial since it offsets sublimation. The first heating step could involve a cross-linking of the Chitosan or PSP-4-PVP polymer, giving a 3D matrix containing the $RhCl_3$ compound linked to the polymeric chain. The following steps could include the beginning of the organic carbonization, producing holes where the nanoparticles begin to nucleate. As confirmed in earlier studies [10, 24], RhO_2 and Rh_2O_3 oxides, and the Rh grow over a layered graphitic carbon host, which is lost near to the final annealing temperature, i.e., 800 °C.

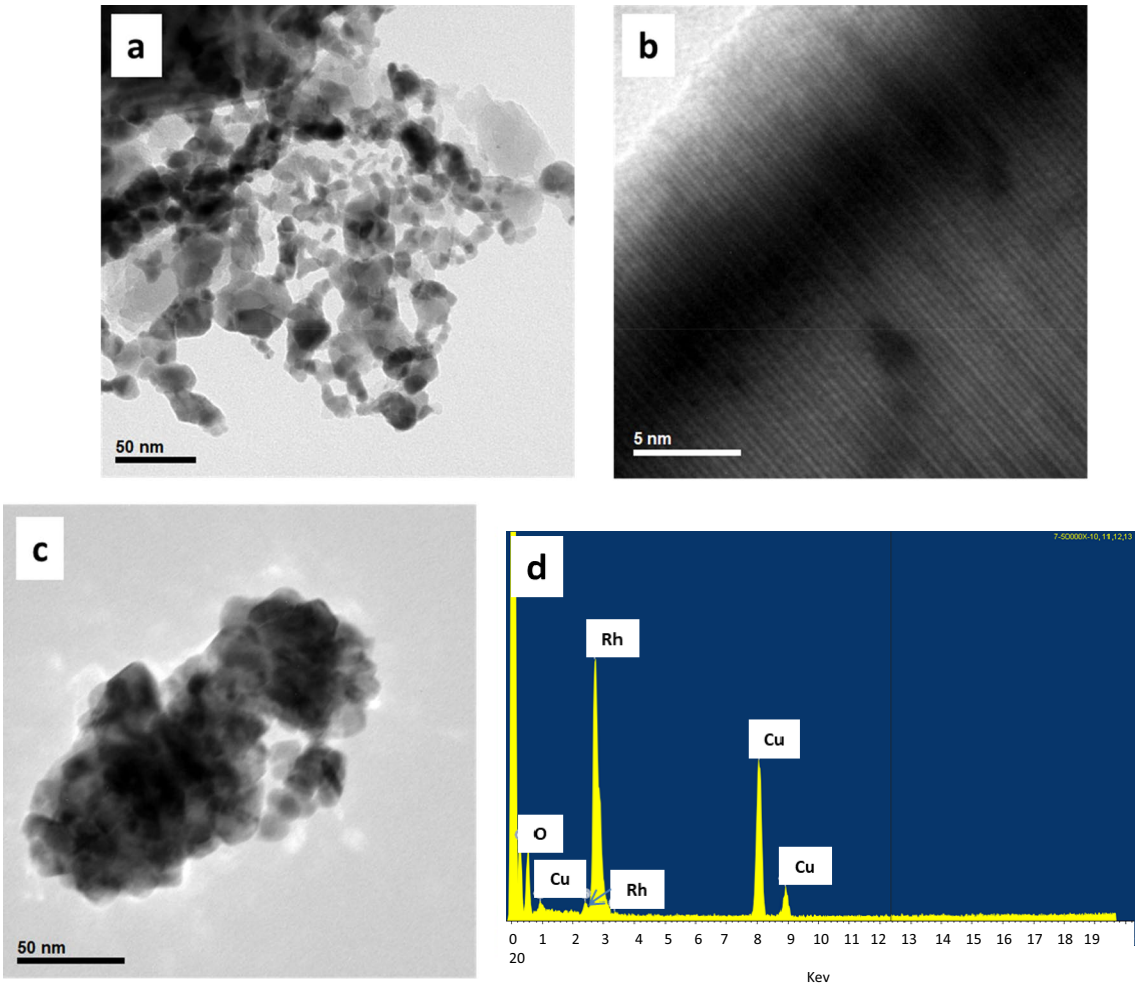

Fig. 3 **a** TEM image showing Rh/Rh_2O_3 particles from the PVP precursor; **b** HR-TEM of a Rh_2O_3 particle from the chitosan precursor showing an interplanar spacing of 0.352 nm (200 plane); **c** TEM image showing agglomerated RhO_2/Rh particles from the chitosan precursor. **d** EDS of the previous image confirming the presence of Rh and oxygen

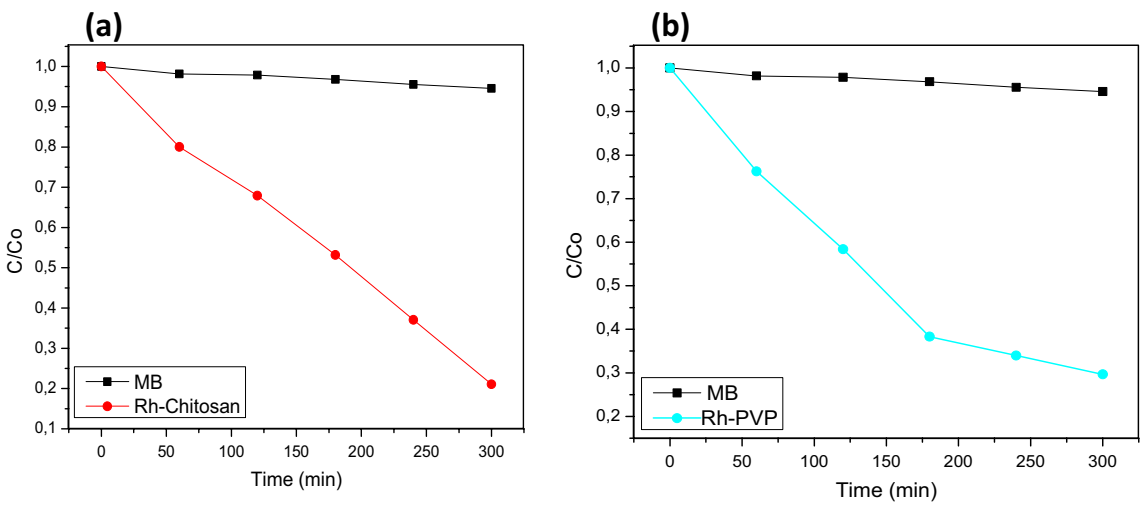

Fig. 4 **a** Normalized MB concentration change without catalyst, in presence of Rh/RhO_2 from Chitosan·$(RhCl_3)_X$ and **b** in presence of Rh/Rh_2O_3 from PSP-4-PVP·$(RhCl_3)_X$

Table 1 Photocatalytic properties and band gap values for several metal oxides

Photocatalyst	Discoloration rate % (time minutes)	Irradiation type	Band gap (eV)	Reference
NiO	71 (300)	UV–visible	4.15	Unpublished results
TiO_2	98 (25 min)	UV	3.7	[25]
ReO_3	53 (300 min)	UV–visible	–[a]	[26]
IrO_2	38 (300 min)	UV–visible	–[a]	[27]
Fe_2O_3	94 (150 min)	UV	2.1	[28]
ThO_2	66 (300 min)	UV–visible	5.66	Unpublished results
Rh/RhO_2	78 (300 min)	UV–visible	3.7	This study
Rh/Rh_2O_3	70 (300 min)	UV–visible	3.0	This study

[a]Not measured

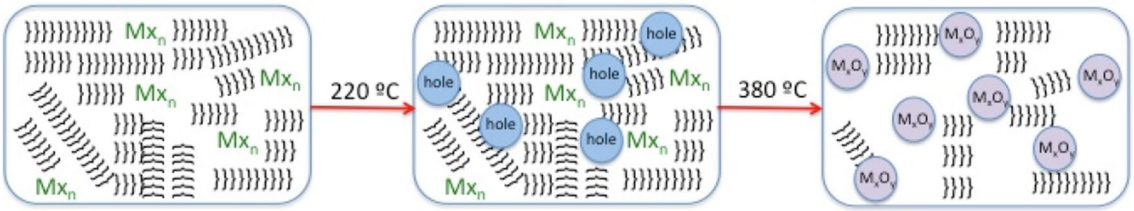

Fig. 5 Schematic representation of the proposed formation mechanism of metal oxide nanoparticles. Each MX_n represents the general formula of the metallic salt coordinated to the Chitosan and PSP-4-PVP polymer, and each}}}}}} represents the Chitosan and PSP-4-PVP polymer. Temperatures are general referential values

4 Conclusions

For the first time, a solid-state control of the oxides RhO_2, Rh_2O_3 phase as well as metallic Rh was observed through the polymer involved in the precursors: a mixture of the nanostructured Rh/RhO_2 phase from the chitosan·$(RhCl_3)_X$ precursor and the Rh/Rh_2O_3 from the PSP-4-PVP·$(RhCl_3)_X$, precursor. The nature of the polymeric precursor, acting as a solid-state template, did not significantly influence the "foam-like" morphology of the Rh metal oxide products. Recently, this solid-state synthesis strategy has been successfully used for doped nanostructured lanthanide oxides [29]. The Rh/RhO_2 and Rh/Rh_2O_3 materials, with 3.7 eV and 3.0 eV bandgaps, respectively, exhibit high photodegradation efficiency toward methylene blue tested for the first time for these rhodium oxides.

Acknowledgements The authors acknowledge Fondecyt Project 1160241 for financial support. This research also received funding from Consejo Superior de Investigaciones Científicas, Spain, under Grant I-COOP LIGHT 2015CD0013. The use of Servicio General de Apoyo a las Investigación (SAI, University of Zaragoza) is also acknowledged.

References

1. F.A. Cotton, G. Wilkinson, *Advanced Inorganic Chemistry, Chapter 22 and 30* (Wiley, New York, 1980)
2. R. Jin, The impacts of nanotechnology on catalysis by precious metal nanoparticles. Nanotechnol. Rev. **1**, 31–56 (2012)
3. M. Fernandez-Garcia, A. Martinez-Arias, J. Hanson, C. Rodriguez, Nanostructured oxides in chemistry: characterization and properties. J. A. Chem. Rev. **104**, 4063–4104 (2004)
4. Y.L. Kim, Y. Ha, N.S. Lee, J.G. Kim, J.M. Baik, C. Le, K. Yoon, Y. Lee, M.H. Kim, Hybrid architecture of rhodium oxide nanofibers and ruthenium oxide nanowires for electrocatalysts. J. Alloys Compd. **663**, 574–580 (2016)
5. J. Bai, S.-E. Han, R. Peng, J.-H. Zheng, J.-X. Jiang, Y. Chen, Ultrathin rhodium oxide nanosheet nanoassemblies: synthesis, morphological stability, and electrocatalytic application. ACS Appl. Mater Interfaces **9**, 17195–17200 (2017)
6. K. Shimura, H. Kawai, T. Yoshida, H. Yoshida, Simultaneously photodeposited rhodium metal and oxide nanoparticles promoting photocatalytic hydrogen production. Chem. Commun. **47**, 8958–8960 (2011)
7. A. Saric, S. Popovic, S. Music, Formation of crystalline phases by thermal treatment of amorphous rhodium hydrous oxide. Mater. Lett. **55**, 145–151 (2002)
8. A. Saric, S. Popovic, R. Trojko, S. Music, The thermal behavior of amorphous rhodium hydrous oxide. J. Alloys. Compd. **320**, 140–148 (2001)

9. L.S. Kibis, A.I. Stadnichenko, S.V. Koscheev, V. Zaikovskii, A.I. Boronin, XPS study of nanostructured rhodium oxide film comprising Rh^{4+} species. J. Phys. Chem. C **120**, 19142–19150 (2016)
10. C. Díaz, M.L. Valenzuela, M.A. Laguna-Bercero, A. Orera, D. Bobadilla, S. Abarca, O. Peña, Synthesis and magnetic properties of nanostructured metallic Co, Mn and Ni oxide materials obtained from solid-state metal-macromolecular complex precursors. RSC Adv. **7**, 27729–27736 (2017)
11. C. Díaz, M.L. Valenzuela, K. Mendoza, O. Peña, C. O´Dwyer, Nanostructured copper oxides and phosphates from a new solid-state route. Inorg. Chim. Acta **377**, 5–13 (2011)
12. C. Diaz, O. Crespo, C. O´Dwyer, C. Gimeno, A. Laguna, I. Ospino, M.L. Valenzuela, Luminescent gold and silver complexes with the monophosphane 1-(PPh_2)-2-Me-$C_2B_{10}H_{10}$ and their conversion to gold micro-and superstructured materials. Inorg. Chem. **54**, 7260–7269 (2014)
13. B. Teo, X. Sun, Silicon-based low-dimensional nanomaterial and nanodevices. Chem. Rev. **107**, 1454–1532 (2007)
14. G.B. Khomutov, V.V. Kislov, M.N. Antipirina, R.V. Gainutdinov, S.P. Gubin, A.Y. Obydenov, S.A. Pavlov, A.A. Rakhnyanskaya, A.N. Sergeev-Cherenkov, E.S. Soldatov, D.B. Suyatin, A.L. Toltikhina, A.S. Trifonov, T.V. Yurova, Interfacial nanofabrication strategies in development of new functional nanomaterials and planar supramolecular nanostructures for nanoelectronics and nanotechnology. Microelectron. Eng. **69**, 373–383 (2003)
15. M.P. Pileni, Self-assembly of inorganic nanocrystals: fabrication and collective intrinsic properties. Acc. Chem. Res. **40**, 685–693 (2007)
16. M.P. Pileni, 2D superlattices and 3D supracrystals of metal nanocrystals: a new scientific adventure. J. Mater. Chem. **21**, 16748–16758 (2001)
17. Y.F. Wan, N. Goubet, P.A. Albouy, M.P. Pileni, Hierarchy in Au nanocrystal ordering in supracrystals: a potential approach to detect new physical properties. Langmuir **29**, 7456–7463 (2013)
18. C. Díaz, M.L. Valenzuela, Metallic nanostructures using oligo and polyphosphazenes as template or stabilizer in solid state, in *Encyclopedia of Nanoscience and Nanotechnology*, vol. 16, ed. by H.S. Nalwa (American Scientific Publishers, Valencia, 2010), pp. 239–256
19. F.P. Koffyberg, Optical bandgaps and electron affinities of semiconducting Rh_2O_3 (I) and Rh_2O_3 (II). J. Phys. Chem. Solids **53**, 1285–1288 (1992)
20. Y. Abe, K. Kato, M. Kawamura, K. Sasaki, Rhodium and rhodium oxide thin films characterized by XPS. Surf. Sci. Spectra **8**, 117 (2001)
21. T.M. Silva, A.M.P. Simoes, M.G.S. Ferreira, M. Walls, M. Da Cunha, BeloElectronic structure of iridium oxide films formed in neutral phosphate buffer solutions. J. Electroanal. Chem. **441**, 5–12 (1998)
22. Y.D. Sherson, S.J. Aboud, J. Wilcoc, B.J. Cantwell, J. Phys. Chem **115**, 11036–11044 (2001)
23. C.-C. Wang, J.-R. Li, X.-L. Lv, Y.-Q. Zhang, G. Guo, Photocatalytic organic pollutants degradation in metal-organic frameworks. Energy Environ. **7**, 2831–2867 (2014)
24. C. Díaz, M.L. Valenzuela, V. Lavayen, C. O´Dwyer, Layered graphitic carbon host formation during liquid-free solid state growth of metal pyrophosphates. Inorg. Chem. **51**, 6228–6236 (2012)
25. P. Allende, M. Laguna, L. Barrientos, M.L. Valenzuela, C. Diaz, Solid state tuning morphology, crystal phase and size through metal macromolecular complexes and its significance in the photocatalytic response. ACS Appl. Energy Mater. **1**, 3159–3170 (2018)
26. C. Diaz, M.L. Valenzuela, O. Cifuentes-Vaca, M. Segovia, M.A. Laguna-Bercero, Incorporation of nanostructured ReO_3 in silica matrix and their activity toward photodegradation of blue methylene. J. Inorg. Organomet. Polym. Mater. **30**, 1726–1734 (2020)
27. C. Diaz, M.L. Valenzuela, O. Cifuentes-Vaca, M. Segovia, M.A. Laguna-Bercero, Iridium nanostructured metal oxide, its inclusion in silica matrix and their activity toward photodegradation of methylene blue. Mater. Chem. Phys. (2020). https://doi.org/10.1016/j.matchemphys.2020.123276
28. C. Diaz, L. Barrientos, D. Carrillo, J. Valdebenito, M.L. Valenzuela, P. Allende, H. Geaney, C. O'Dwyer, Solvent-less method for efficient photocatalytic α-Fe_2O_3 nanoparticles for using macromolecular polymeric precursors. New J. Chem. **40**, 6768–6776 (2016)
29. C. Díaz, M.L. Valenzuela, C. Garcia, R. de la Campa, A.-P. Soto, Solid-state synthesis of pure and doped lanthanides oxide nanomaterials by using polymer templates. Study of their luminescent properties. Mater. Lett. **209**, 111–114 (2017)